Effect of Octahedral Connectivity on the

Negative Thermal Expansion of SrZrS₃

Nathan Z. Koocher and James M. Rondinelli*

Department of Materials Science and Engineering, Northwestern University, Evanston,
Illinois 60208, USA

E-mail: jrondinelli@northwestern.edu

Abstract

Sulfide perovskites (ABX_3) are under increasing investigation for use in photovoltaic, optoelectronic, dielectric, and thermoelectric devices due to their favorable band gaps, dynamical properties, environmental stability, and structural diversity. A key material parameter to optimize in such devices is the constituent materials' coefficient of thermal expansion (CTE) in order to minimize thermomechanical stress during fabrication and operation. This can be done by avoiding materials that have large CTE mismatch or to compensate positive thermal expansion by including materials with negative thermal expansion (NTE). Here, we evaluate the CTE of (edge-connected) α - and (corner-connected) β -SrZrS₃ with density functional theory and the self-consistent quasiharmonic approximation. We find that both materials exhibit positive thermal expansion at 0 GPa and host pressure-induced negative thermal expansion. The β phase has a smaller CTE ($37 \times 10^{-6} \text{ K}^{-1}$) at room temperature and ambient pressure, also has a larger NTE response under pressure due to its more flexible corner-connected framework structure. We use our findings to suggest that corner-shared motifs should be prioritized over edge- or face-shared octahedral networks to maximize NTE arising from vibrational (phononic) mechanisms.

Introduction

Thermal expansion is a critical property to manage when fabricating and operating electronic devices, as mismatch of the thermal expansion coefficients (CTE) from different components can cause thermal stresses, leading to device failure via delamination at interfaces and wiring failures. Mitigation of mismatch and thermal stresses is done via the inclusion of materials with negative thermal expansion (NTE) —the phenomena wherein a material contracts when heated. This strategy has recently been used in solid oxide fuel cells to better match CTEs of the electrode and electrolyte. Chalcogenide perovskite materials have recently been investigated in photovoltaic, dielectric, thermoelectric, and fuel cell applications due to their environmental stability, and favorable electronic and lattice dynamical properties, but their thermal expansion behaviour is not well understood.

Many chalcogenide studies have focused on the distorted perovskite (GdFeO₃-type) or perovskite-derived Ruddlesden Popper phases, but these ternary compounds can also form 10,11 in a hexagonal phase (BaNiO₃-type) and non-perovskite, needle-like phase (NH₄CdCl₃-type). These structures exhibit different connectivity of their octahedra: corner-shared for distorted perovskite, face-shared for hexagonal perovskite, and edge-shared for the needle-like phase. Some compounds, like SrZrS₃, have been synthesized in both the needle-like (α) and distorted perovskite (β) phases. ¹² Exploring phases beyond the distorted perovskite is important because they may also have desirable properties for device applications. For example, Shahmohemadi and Naghavi found that both distorted perovskite BaHfS₃ and needle-like SnHfS₃ were promising thermoelectrics based on their large power factors and low lattice thermal conductivities.⁷

Similarly, most negative thermal expansion work has focused on oxide and fluoride framework structures with corner-shared octahedra. ¹³ Although compounds with edge-connected motifs (often creating one dimensional chains) also exhibit this property, they usually have corner-connected motifs in their structures as well. Examples include $A_2M_2O_7$, ^{14–17} $A_2O(MO_4)_2^{18-20}$ oxides, fluorine-excess double ReO₃-type fluorides (MM'F₆ structral deriva-

tives), ^{21–23} and ZnF₂ ^{24,25} (rutile-type). ²⁶ From Table 1 of the review by Shi et al., ²⁶ structures with mixed corner- and edge-shared polyhedra exhibit smaller negative magnitudes of the CTE than those with only a corner-shared motif. Additionally, upon incorporation of excess fluorine in some double ReO₃-type fluorides, some corner-shared octahedra are converted to edge-shared octahedra and the NTE response is suppressed. ^{21–23} Although edge connectivity appears to hinder NTE in these compounds, it is an open question whether a fully edge-connected structure could host NTE, and if so, what the mechanism would be, e.g., an often seen transverse vibration or something akin to the quasi-2D vibrations found in some Ruddlesden-Popper compounds. ^{27,28}

Here we compute and compare the volumetric thermal expansion of edge-shared α -SrZrS₃ and β -SrZrS₃ using density functional theory (DFT) and the self-consistent quasiharmonic approximation method. These polymorphs have the same space group, but represent extremes in metal-anion octahedral connectivity: only edge-connected (α) or only corner-connected (β). We find that both compounds exhibit positive volumetric thermal expansion (PTE) at 0 GPa, but develop NTE under pressure. β -SrZrS₃ has a phononic quasi-RUM (qRUM) mechanism like that in isostructural CaTiO₃, ²⁸ whereas the NTE in α -SrZrS₃ is due to bending of the apical Zr-S bonds in its ZrS₆ octahedra. Our results show edge-connectivity provides control over the microscopic mechanism of pressure-induced NTE.

Methods

DFT calculations were performed with VASP, 29,30 utilizing the PBEsol exchange correlation functional 31 and PAW pseudopotentials. 32,33 The valence configurations were $4s^24p^65s^2$ for Sr, $4s^24p^65s^14d^3$ for Zr, and $3s^23p^4$ for S. The energy cutoff for the plane wave basis used in all calculations was 600 eV. For all relaxations, the energy convergence criteria was 1×10^{-8} eV and the force convergence criteria was 1×10^{-5} eV Å⁻¹. An $8\times6\times4$ Γ -centered k-point grid was used for the α phase and a $6\times6\times4$ grid for the β phase. Also, a Gaussian smearing method

with a smearing value of 0.1 eV was used for all calulations. Phonon spectra were computed using the finite displacement method implemented with the PHONOPY code.³⁴ For both polymorphs, the displacement amplitude was 0.03 Å. A $3\times2\times2$ supercell was used for the α -phase and a $2\times2\times2$ supercell was used for the β -phase force constant calculations. An energy convergence criteria of 1×10^{-7} eV was used for the phonon calculations. Using the phonons as input, the thermomechanical properties were then generated with the self-consistent quasiharmonic approximation (SC-QHA).³⁵

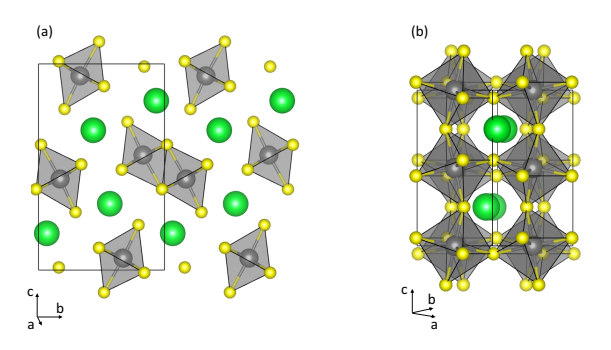


Figure 1: Structures of (a) α -SrZrS₃ and (b) β -SrZrS₃. Both have the *Pbnm* space group, however the α phase has edge-connected ZrS₆ octahedra, while the β phase has corner-connected ZrS₆ octahedra. Sr: green spheres, Zr: gray spheres in octahedra, S: yellow spheres.

Results

Crystallographic Structures

Figure 1 shows the (a) α -SrZrS₃ polymorph and (b) β -SrZrS₃ polymorph. We find that the α phase is 46.3 meV per formula unit more stable than the β -phase at 0 K in our DFT calculations of the equilibrium structures. When we include the entropic contribution from the phonons, we find that α -SrZrS₃ remains more stable up to 590 K (see the Supporting Information and Figure S1). For T > 590 K, the β phase becomes more energetically stable. Based on the free energy differences, we expect that structural conversion from the α -phase to the (lower free energy) β -phase at higher temperatures may occur through a reconstructive

Table 1: DFT computed structure data for α and β SrZrS₃. The average (avg.) local structure, i.e., bond lengths (Å) and polyhedral volumes (Å³), are similar. The lattice constants are reported in Å.

Structural Features	α	β
a	3.79	6.68
b	8.45	7.11
c	13.82	9.73
Volume	443.22	462.25
Avg. Zr-S bond length	2.56	2.54
Avg. Zr-S apical bond length	2.54	2.52
Avg. Zr-S equatorial bond length	2.57	2.55
$Avg. ZrS_6$ octahedral volume	22.20	21.93

transition owing to the different octahedral connectivity which requires bond reorganization. Note that while both phases are stable at room temperature experimentally, the α -phase oxidizes at 550°C (823 K) upon heating in air, while the β -phase oxidizes at 650°C (923 K).

Both phases exhibit Pbnm orthorhombic symmetry, but the α -phase has a notably shorter a-axis of 3.79 Å (Table 1). Both phases comprise ZrS_6 octahedra, although with different connectivity. The α phase has quasi-1D chains of edge-connected ZrS_6 octahedra extending along the a axis. The chains are arranged in a disconnected row along the b axis, with each chain pointing in the same direction (tilted 28.0° off of the b axis). Each chain has a width of two (edge-connected) octahedral units. The columns are also disconnected along the c axis, where each we see that the chains have an ABAB tilt pattern. The Sr atoms are interspersed between the columns both in-plane and out-of-plane. The β -phase exhibits 3D corner connected ZrS_6 octahedra connected in all directions. It is described as a perovskite with Glazer notation $a^-a^-c^+$ with an octahedral rotation angle of 12.5° along [001] and a tilt angle of 10.4° along [110].

Phonon Dispersions

Figure 2 shows the ambient pressure phonon dispersions for the two polymorphs. The atomand direction-resolved phonon projected density of states (PDOS) are given in Figures S2 and

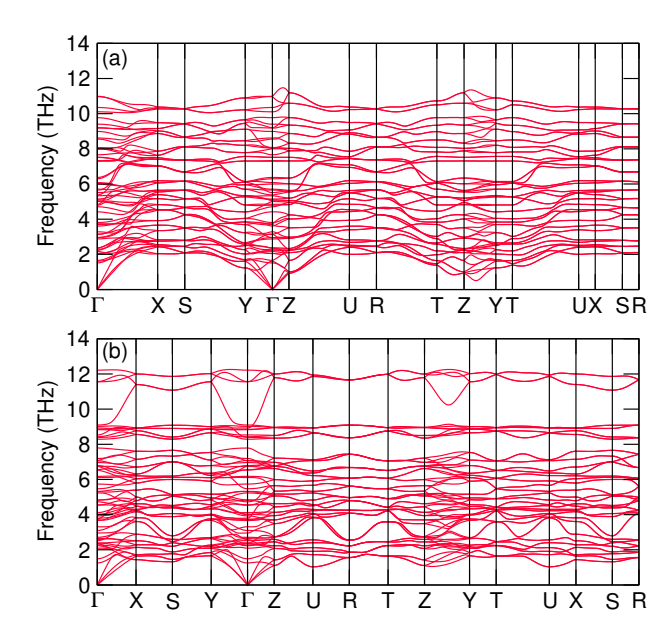


Figure 2: Phonon band structures of (a) α -SrZrS₃ and (b)- β SrZrS₃.

S3. Because both compounds have the same space group we can plot the phonon dispersions in momentum space using the same reciprocal space path; the paths are of different lengths, however, because the lattice constants differ. Although the α phase has a smaller volume, we find that it has lower-frequency modes than the β phase. Detailed analysis of the phonon dispersions shows that most of the β -phase modes (57/60 of them with frequencies < 9.2 THz) are lower in frequency than the α -phase modes as expected. The 3 that are higher in frequency in the range 11-12.2 THz are octahedral breathing modes dominated by sulfur displacements. Owing to the connectivity difference (disconnected edge-shared columns for the α phase and a 3D-corner connected network for the β phase), these breathing modes do not have direct correspondence in the edge-connected α phase.

Upon examining the atom-resolved phonon PDOS (Figure S2), we find that Sr has a low-frequency peak at approximately 2.5 THz in both structures. Sr contributes to phonon modes that extend up to approximately 6 THz in the α phase and 7.5 THz in the β phase. There is Zr-S overlap throughout the frequency range for both phases, reflecting strong Zr-S vibrational coupling in the covalent Zr-S motifs (column or framework, respectively). The α phase has a Zr peak at about 2.5-3 THz, while there is a broader dispersion of Zr

density below 7.5 THz in the β phase. Regarding the direction-resolved PDOS (Figure S3), both polymorphs exhibit overlapping peaks from X-, Y-, and Z directions, indicating strong vibrational coupling in all directions. This is consistent with the patterning of columns in the α phase in 3D as well as 3D octahedral connectivity in the β phase.

Grüneisen Dispersions

Having established that both phases are dynamically stable at 0 K in our DFT calculations, we now analyze the corresponding Grüneisen parameters associated with each mode, which we refer to as the mode-Grüneisen parameters (γ). These quantities describe how phonon frequencies respond to volume changes, and are calculated as

$$\gamma_i = -\frac{V}{\omega_i} \frac{\partial \omega_i}{\partial V} \,, \tag{1}$$

where V is the volume of the unit cell, ω_i is the phonon frequency of phonon i, and γ_i is the Grüneisen parameter for phonon i.³⁷ If a mode has a negative Grüneisen parameter, it means its frequency decreases (i.e., softens) in response to volume compression. Conversely, if a mode has a positive Grüneisen parameter, then its frequency increases (i.e., hardens) in response to volume compression.³⁷ Usually a volumetric compression in this manner is achieved with hydrostatic pressure. Modes that soften with applied pressure, and hence have negative Grüneisen parameters, usually exhibit transverse motion of atoms in their corresponding eigendisplacement pattern. In contrast, modes that harden with pressure and have positive Grüneisen parameters usually exhibit bond stretching in their corresponding displacement pattern.²

Figure 3 presents the Grüneisen dispersion of both phases and presents mainly those modes with negative values. In the α phase, there are 4 modes that yield negative Grüneisen parameters of similar value: the Z-direction acoustic (ZA), transverse acoustic (TA), longitudinal acoustic (LA) and shearing optical (SO) modes. All modes have a positive (γ^+) to

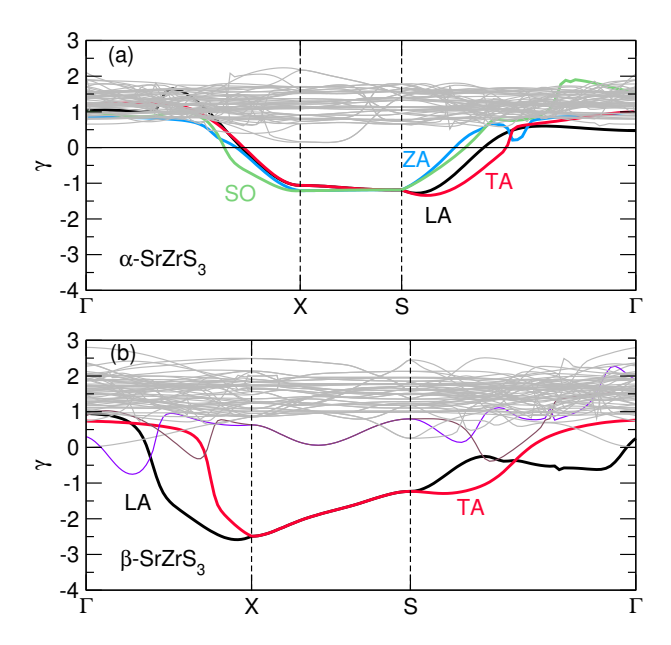


Figure 3: Mode Grüneisen parameters of (a) α -SrZrS₃ and (b) β -SrZrS₃. Modes causing NTE have negative values on the ordinate axis and are highlighted. Notation is as follows: ZA, Z-direction acoustic; TA, transverse acoustic; LA, longitudinal acoustic; and SO, shearing optical.

negative (γ^-) transition along the Γ -X path. This occurs due to initial bond stretching in the displacement pattern of all modes near the Γ -point. The character than changes with an increase in bond bending along the path until there is apical S-Zr-S bond bending in the octahedra of the quasi-1D chains at the X-point, resulting in γ^- . Figure S4 illustrates the apical S-Zr-S motion.

In the β phase, there are two dominant modes yielding negative Grüneisen parameters, the LA and TA modes. Note that these modes are similar to those of the α phase in notation only; the character of the displacements differ because of the different connectivity of the atoms. Both of these modes have a γ^+ to γ^- transition along the Γ -X path as well, which is due to initial bond stretching followed by an increasing amount of bond bending. For this polymorph, the LA and TA modes are degenerate at the X-point where there is strong in-plane and out-of-plane S-Zr-S bond bending, resulting in a quasi-RUM (qRUM) motion which is shown in Figure S4 and the supplemental videos. Based on this analysis, we attribute the larger negative Grüneisen values for the β phase, as compared to the α phase, to the

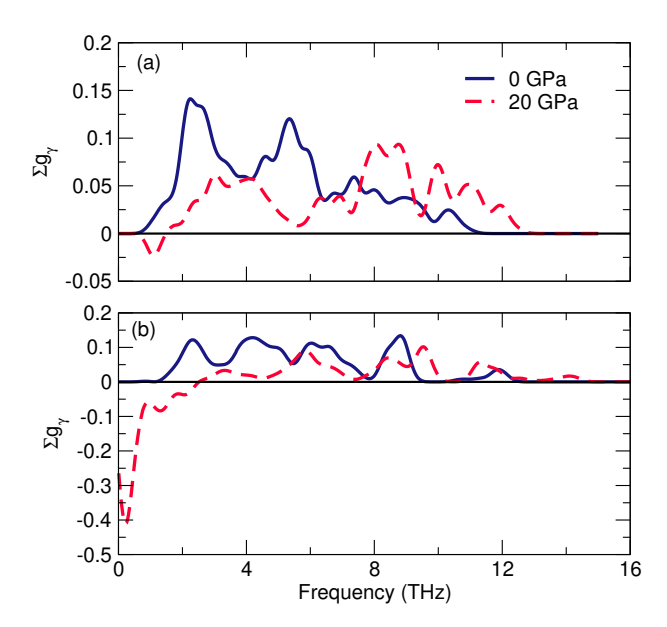


Figure 4: The Gruneisen-weighted phonon density of states γ_g of (a) α SrZrS₃ and (b) β SrZrS₃ at ambient conditions (0 GPa) and under pressure (20 GPa).

larger bond bending found in the qRUM motion from the corner-connected octahedra. The α phase, in contrast, has only apical bond bending vibrations because of the edge-connected octahedra which excludes in-plane bond bending.

To discern the pressure effect on the mode Grüneisen parameters, we compute the Grüneisen-weighted phonon density of states:

$$g_{\gamma^{\pm}}(\nu) = \frac{1}{N_q} \sum_{q,\sigma} \gamma_{q,\sigma}^{\pm} \delta(\nu - \nu_{q,\sigma})$$
 (2)

In the equation, q and σ of the summation enumerate the phonon wave vector and branch, respectively, γ^{\pm} is the mode Grüneisen parameters (of positive (+) or negative (-) value) corresponding to a phonon of frequency ν (both indexed by phonon wave vector and branch), and N_q is the number of grid points. The summation and delta function represent a count of phonons at a given frequency, i.e., the phonon density of states $g(\nu)$, which is weighted by the Grüneisen parameter values for each phonon, $g_{\gamma^{\pm}}(\nu)$. The positive $(g_{\gamma^{+}})$ and negative $(g_{\gamma^{-}})$ densities of states are summed per frequency point into a total $\sum g_{\gamma}$ and plotted to more easily illustrate the pressure effect (Figure 4). For both phases, there is only positive $g_{\gamma^{+}}$ at 0

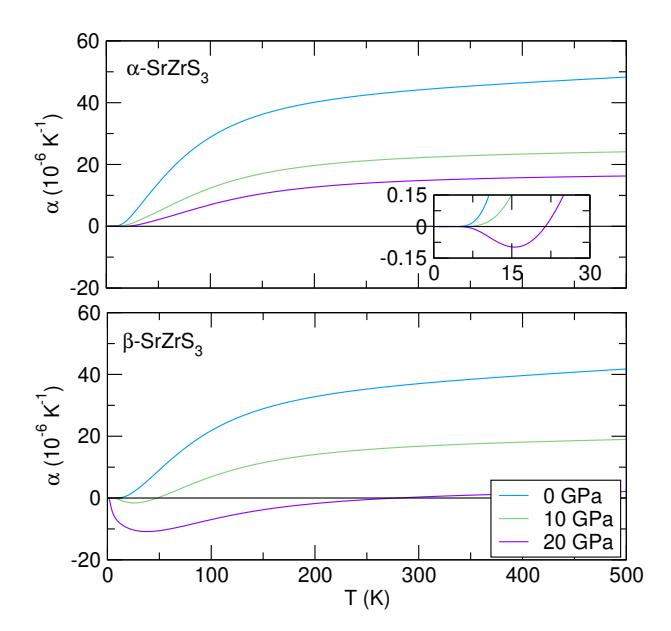


Figure 5: Pressure-dependent CTE of (a) α -SrZrS₃ and (b) β -SrZrS₃. Both phases have PTE ($\alpha > 0$) at ambient pressure but develop NTE ($\alpha < 0$) under pressure.

GPa. At 20 GPa, the γ^+ modes blueshift to higher frequency while the γ^- modes redshift to lower frequency, resulting in net negative g_{γ^+} at low frequencies for both polymorphs (\sim 1 THz in the α phase and 0.4 THz in the β phase). Consistent with the previously discussed mode Grüneisen parameter plots and displacements, the β phase exhibits greater negative g_{γ^+} than the α phase.

Thermal Expansion

The simulated volumetric temperature dependent thermal expansion α are shown in Figure 5. Both phases exhibit positive thermal expansion (PTE) at 0 GPa with pressure-induced negative thermal expansion (NTE). At ambient pressure and 300 K, the α phase has a larger CTE than the β phase (44 × 10⁻⁶ K⁻¹ compared to 37 × 10⁻⁶ K⁻¹, respectively). A recent x-ray diffraction experiment showed that the CTE of β -SrZrS₃ from 300-900 K is approximately 36 × 10⁻⁶ K⁻¹,³⁸ which compares well with our simulated value at 300 K. We could not find experimental data for α -SrZrS₃. To describe the NTE response of the two materials, we denote the critical pressure, p_c as the pressure at which there is some occurence of a negatively valued thermal expansion coefficient (α) in the temperature range simulated.

Moreover, we denote the critical temperature T_c as the upper temperature bound of the NTE region at a given pressure where $\alpha(T_c) = 0$. In the α phase, these values are $p_c = 20$ GPa with a corresponding $T_c = 25$ K, while for the β phase they are $p_c = 5$ GPa and corresponding $T_c = 25$ K. The integrated NTE capacity, defined as $\tilde{\chi} = \int_{T_1}^{T_c} \alpha(T) dT$ is greater for the β phase than the α -phase (Figure 6), owing to the larger negative Grüneisen values of the β phase. Finally, pressure reduces the PTE portion of the CTE due to bulk modulus stiffening (see the SI for the bulk moduli).

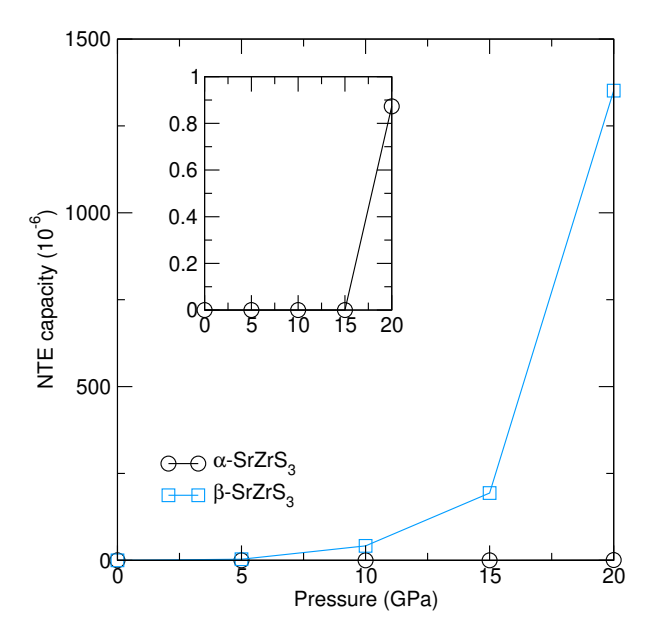


Figure 6: Integrated NTE capacity for the SZS phases as a function of pressure. The β phase has the larger NTE response, which increases as pressure increases.

Discussion

The NTE response of volumetric phonon-driven NTE materials can usually be compared on the basis of bond strength (i.e., stiffness)^{27,39} or elastic constants.^{28,40,41} The material with stronger bonds or higher elastic constants (i.e., the stiffer material) would have a lower NTE response. In this case, the values for the octahedral bonds are similar and they thus do not predict the NTE response well. Additionally, the α phase has a lower bulk modulus than the β phase over all temperatures calculated. Here, the difference in NTE response is due to

the difference in octahedral connectivity, as shown in the Grüneisen dispersion analysis. The edge-connection in the α -phase constricts the bond bending, resulting in a lower negative Grüneisen parameter and thus lower negative thermal expansion response than the more pliable corner-connected β phase.

Although most known network structures that display NTE have corner-connected frameworks, the oxide families $A_2M_2O_7$ and $A_2O(PO_4)_2$ as well as fluorine-excess double ReO₃-type fluorides (MM'F₆ derivatives) and ZnF₂ (rutile) have edge-connected polyhedra and show NTE. ²⁶ $A_2M_2O_7$ materials have edge-connected AO_5 polyhedra and corner-connected MO₄ tetrahedra, and interestingly, the transverse vibrations of the corner-connected oxygen in the tetrahedra mostly drive the NTE. ^{14–17,26} The $A_2O(PO_4)_2$ family has both edge-connected AO_7 polyhedra forming chains, which have phosphate PO_4 tetrahedra connected to it in an alternating edge-connected and corner-connected manner (via oxygen atoms in both cases). ²⁶ The NTE is driven both by transverse vibration of corner-connected oxygen atoms as well as a ring deformation due to Coulombic interactions causing a Poisson-type effect. ^{18,19} It is important to note that there is local (positive) expansion from cations sharing an edge due to Coulombic repulsion. ²⁰ In both of these oxide families, corner-connected subunits play a dominant or important role in causing the NTE, which is consistent with longstanding mechanistic expectations in the field. ¹³ This agrees with our simulations that the corner-connected β phase has a higher NTE response than the edge-connected α phase.

The MM'F₆ fluorides exhibit the ReO₃-type structure with corner-connected, alternating MF₆ and M'F₆ octahedra. They have NTE in their cubic $Fm\bar{3}m$ phases due to the rocking of the octahedra; the magnitude of the NTE response can be tuned by changing bond strengths via chemical substitution. When excess fluoride is included in some of these materials, a fraction of the corner-connected octahedra transform to edge-connected polyhedra and inhibit the NTE.²⁶ In Mg_{1-x}Zr_{1+x}F_{6+2x}, for example, excess fluorine first enhances the NTE by stabilizing the $Fm\bar{3}m$ structure against a temperature phase transition (at x=0.15), but then inhibits the NTE as the fluorine concentration increases (x=0.30, 0.40, 0.50).²¹ The

excess fluorine atoms reside at interstitial sites and promote some edge-sharing between polyhedra (formerly octahedra), inhibiting the concerted rocking of the polyhedra with temperature, thus reducing the NTE response. ²¹ Conversely, fluorine removal from fluorine-excess ReO₃-type ($Fm\bar{3}m$ space group) TiZrF_{7-x} caused NTE. ²³ TiZrF₇ had PTE with a $\alpha = 8.07 \times 10^{-6} \text{ K}^{-1}$, TiZrF_{6.5} had a smaller PTE with $\alpha = 0.66 \times 10^{-6} \text{ K}^{-1}$, and TiZrF₆ had NTE with $\alpha = -6.09 \times 10^{-6} \text{ K}^{-1}$. ²³ The change in response was due to greater availability of the polyhedra to freely rotate as edge-connected units transformed to corner-connected units, thereby promoting NTE. ²³ Note that a similar NTE-tuning mechanism is behind the NTE-to-PTE modulation in Zr-doped ScF₃. ^{42,43} From these studies, we conclude that NTE is suppressed as there is a greater number of edge-shared polyhedra, which is consistent with our results on SrZrS₃.

ZnF₂, on the other hand, has edge-connected ZnF₆ octahedra along its short c axis and these chains are corner-connected in the ab plane. ²⁶ Volumetric NTE appears experimentally at temperatures below 75 K and the CTE reaches a minimum of about -2 × 10⁻⁶ K⁻¹ at 30 K. ²⁴ If contributions are decomposed by axis, however, NTE occurs along the in-plane direction, but PTE is found along the edge-connected c axis. ²⁴ Theoretical analysis using DFT calculations attributed the volumetric NTE to a rigid unit mode mechanism from the octahedra. ^{24,25} Thus, corner-connected motifs generate the NTE in ZnF₂, and the microscopic mechanism is consistent with those of other framework materials. ¹³ This finding supports the larger response of the corner-connected β SrZrS₃ than the edge-connected α SrZrS₃ polymorph although for the sulfide both motifs do display NTE under pressure.

We can now compare the NTE response of the β SrZrS₃ to isostructural CaTiO₃ detailed in our previous work. ²⁸ Both materials exhibit the same phononic mechanism—LA and TA phonon modes yielding negative Grüneisen parameters due to their quasi-RUM vibrational pattern at the X-point in the Brillouin zone. Interestingly, the response of the sulfide is much larger and appears at a lower NTE critical pressure: p_c is 5 GPa for the sulfide but 20 GPa for the oxide. In addition, the NTE capacity is 1351 for the sulfide but only 0.21 for the oxide. We understand this behavior as follows. The sulfide is the less rigid compound, evidenced by its longer bonds (2.54 Å for β SrZrS₃ vs. 1.96 Å for CaTiO₃) and its lower bulk modulus (67.3 GPa for the sulfide and 161.5 GPa for the oxide). Its NTE-generating phonon modes at the X-point, furthermore, occur at lower frequency (1.44 THz for the sulfide and 3.06 THz for the oxide) owing to the larger unit cell volume and heavier masses of the elements in the sulfide. Although A- and B-cation substitution was previously shown to modulate the volumetric²⁷ and uniaxial⁴⁴ NTE response of perovskite derivative n=2 and n=1 Ruddlesden-Popper compounds, respectively, we show here that anion substitution also achieves this control as well.

Furthermore, our work gives two more material examples highlighting pressure as a control vector for the CTE. Our results in both polymorphs wherein the positive-valued CTE is suppressed and negative-valued CTE is enhanced with pressure is consistent with the usual thermodynamic relation of the variation in thermal expansion coefficient with pressure:³⁷

$$\left(\frac{\partial \alpha_V}{\partial P}\right)_T = \frac{1}{B^2} \left(\frac{\partial B}{\partial T}\right)_P \tag{3}$$

where α_V is the volumetric thermal expansion coefficient, B is the bulk modulus, P is pressure, and T is temperature. As Dove and Fang state, the bulk modulus is positive, while the variation in B with T is usually negative such that $\left(\frac{\partial \alpha_V}{\partial P}\right)_T$ will be negative regardless of the sign of α_V .³⁷ Although not seen here, we note that pressure can control the NTE of a material indirectly via phase control. For example, many double ReO₃-type fluorides (MM'F₆) show NTE in their cubic phase, but PTE in the pressure-induced symmetry-lowered phase (often rhombohedral or amorphous). ^{45–49} Moreover, NTE materials may display pressure-induced softening - the material becomes softer instead of harder under compression - which is a complementary area of research. ³⁷

In an applied context, the CTE has been identified as a key material parameter for the processing of thermoelectric materials.⁵⁰ Although there has been recent interest in chalcogenide perovskites for thermoelectrics, with in-depth studies of corner-connected CaZrSe₃, ⁵¹ BaZrS₃, ^{52,53} and CaZrS₃, ^{54,55} a comprehensive screening and analysis of cornerand edge-shared structures, ⁷ along with their thermal expansion is lacking. For example, the CTE of PbTe-based thermoelectric materials is 20-24 (10^{-6} K⁻¹). Thus, the lower CTE of the β phase relative to the α phase at ambient pressure and room temperature and beyond suggests it may be more suitable for integration into future devices. In addition, Shahmohamadi and Nadhavi showed that the β -phase of SrZrS₃, SrHfS₃, BaZrS₃, and BaHfS₃ have higher power factors than their respective α phases, making them more suitable for thermoelectric applications. ⁷

Conclusion

We simulated the thermal expansion coefficient of $SrZrS_3$ polymorphs and showed that both exhibit PTE at 0 GPa and NTE under pressure. The corner-connected β phase has a larger NTE response due to its more flexible structure, which accommodates larger magnitude transverse vibrations. It also has a similar phononic NTE mechanism to isostructural CaTiO₃. The edge-connected octahedra in the α phase constrain transverse movement of equatorial Zr-S bonds. As opposed to many examples in literature, these polymorphs have only one type of octahedral bonding and allowed us to isolate the effect of edge-connectivity on NTE. Given the smaller CTE at room temperature (and at ambient pressure), these results also suggest that corner-connected β -SrZrS₃ phase may be more suitable than the α -SrZrS₃ for technological applications.

Acknowledgement

This work was supported by the National Science Foundation under grant number DMR-2011208. Computational support was provided by DOD HPCMP.

Supporting Information Available

The Supporting Information is available free of charge on the ACS Publications website at DOI: [Link to be inserted].

Free energy analysis of the α - and β -SrZrS₃ polymorph; atom- and direction-resolved phonon density of states; phonon eigenvector images and qRUM videos for modes with negative Grüneisen parameters; simulated and experimental structural data for SrZrS₃; equations-of-state; bulk moduli.

References

- (1) Takenaka, K. Progress of Research in Negative Thermal Expansion Materials: Paradigm Shift in the Control of Thermal Expansion. Frontiers in Chemistry 2018, 6.
- (2) Barrera, G. D.; Bruno, J. A. O.; Barron, T. H. K.; Allan, N. L. Negative Thermal Expansion. *Journal of Physics: Condensed Matter* **2005**, *17*, R217–R252.
- (3) Zhang, Y.; Chen, B.; Guan, D.; Xu, M.; Ran, R.; Ni, M.; Zhou, W.; O'Hayre, R.; Shao, Z. Thermal-Expansion Offset for High-Performance Fuel Cell Cathodes. *Nature* **2021**, *591*, 246–251.
- (4) Swarnkar, A.; Mir, W. J.; Chakraborty, R.; Jagadeeswararao, M.; Sheikh, T.; Nag, A. Are Chalcogenide Perovskites an Emerging Class of Semiconductors for Optoelectronic Properties and Solar Cell? *Chemistry of Materials* 2019, 31, 565–575.
- (5) Bennett, J. W.; Grinberg, I.; Rappe, A. M. Effect of Substituting of S for O: The Sulfide Perovskite BaZrS₃ Investigated With Density Functional Theory. *Phys. Rev. B* 2009, 79, 235115.
- (6) Filippone, S.; Zhao, B.; Niu, S.; Koocher, N. Z.; Silevitch, D.; Fina, I.; Rondinelli, J. M.;

- Ravichandran, J.; Jaramillo, R. Discovery of Highly Polarizable Semiconductors BaZrS₃ and Ba₃Zr₂S₇. *Phys. Rev. Materials* **2020**, 4, 091601.
- (7) Shahmohamadi, H.; Naghavi, S. S. Sulfide Perovskites for Thermoelectricity. *ACS Applied Materials & Interfaces* **2021**, *13*, 14189–14197.
- (8) Polfus, J. M.; Norby, T.; Bredesen, R. Protons in Oxysulfides, Oxysulfates, and Sulfides: A First-Principles Study of La₂O₂S, La₂O₂SO₄, SrZrS₃, and BaZrS₃. The Journal of Physical Chemistry C 2015, 119, 23875–23882.
- (9) Sopiha, K. V.; Comparotto, C.; Márquez, J. A.; Scragg, J. J. S. Chalcogenide Perovskites: Tantalizing Prospects, Challenging Materials. Advanced Optical Materials 2022, 10, 2101704.
- (10) Jess, A.; Yang, R.; Hages, C. J. On the Phase Stability of Chalcogenide Perovskites. Chemistry of Materials 2022, 34, 6894–6901.
- (11) Brehm, J. A.; Bennett, J. W.; Schoenberg, M. R.; Grinberg, I.; Rappe, A. M. The Structural Diversity of ABS₃ Compounds With d⁰ Electronic Configuration for the B-cation. The Journal of Chemical Physics 2014, 140, 224703.
- (12) Lee, C.-S.; Kleinke, K. M.; Kleinke, H. Synthesis, Structure, and Electronic and Physical Properties of the Two SrZrS₃ Modifications. *Solid State Sciences* **2005**, *7*, 1049–1054.
- (13) Sleight, A. W. Compounds That Contract on Heating. *Inorganic Chemistry* **1998**, *37*, 2854–2860.
- (14) Zhang, N.; Li, L.; Wu, M.; Li, Y.; Feng, D.; Liu, C.; Mao, Y.; Guo, J.; Chao, M.; Liang, E. Negative Thermal Expansion and Electrical Properties of α-Cu₂V₂O₇. Journal of the European Ceramic Society 2016, 36, 2761–2766.
- (15) Shi, N.; Sanson, A.; Venier, A.; Fan, L.; Sun, C.; Xing, X.; Chen, J. Negative and Zero

- Thermal expansion in α -(Cu_{2x}Zn_x)V₂O₇ Solid Solutions. *Chem. Commun.* **2020**, *56*, 10666–10669.
- (16) Wang, H.; Yang, M.; Chao, M.; Guo, J.; Gao, Q.; Jiao, Y.; Tang, X.; Liang, E. Negative Thermal Expansion Property of β-Cu₂V₂O₇. Solid State Ionics **2019**, 343, 115086.
- (17) Shi, N.; Sanson, A.; Gao, Q.; Sun, Q.; Ren, Y.; Huang, Q.; de Souza, D. O.; Xing, X.; Chen, J. Strong Negative Thermal Expansion in a Low-Cost and Facile Oxide of Cu2P2O7. Journal of the American Chemical Society 2020, 142, 3088–3093.
- (18) Wallez, G.; Launay, S.; Quarton, M.; Dacheux, N.; Soubeyroux, J.-L. Why Does Uranium Oxide Phosphate Contract On Heating? *Journal of Solid State Chemistry* **2004**, *177*, 3575–3580.
- (19) Wallez, G.; Bregiroux, D.; Quarton, M. Mechanism of the Low Thermal Expansion in α-Hf₂O(PO₄)₂ and Its Zirconium Analog. Journal of Solid State Chemistry 2008, 181, 1413–1418.
- (20) Wallez, G.; Clavier, N.; Dacheux, N.; Bregiroux, D. Negative Thermal Expansion in Th₂O(PO₄)₂. *Materials Research Bulletin* **2011**, 46, 1777–1780.
- (21) Baxter, S. J.; Hester, B. R.; Wright, B. R.; Wilkinson, A. P. Controlling the Negative Thermal Expansion and Response to Pressure in ReO₃-type Fluorides by the Deliberate Introduction of Excess Fluoride: $Mg_{1-x}Zr_{1+x}F_{6+2x}$, x = 0.15, 0.30, 0.40, and 0.50. Chemistry of Materials **2019**, 31, 3440–3448.
- (22) Yang, C.; Zhang, Y.; Bai, J.; Tong, P.; Lin, J.; Tong, H.; Zhang, L.; Wen, W.; Zhang, X.; Sun, Y. Isotropic Low Thermal Expansion over a Wide Temperature Range in Ti_{1-x}Zr_xF_{3+x} (0.1 ≤ x ≤ 0.5) Solid Solutions. *Inorganic Chemistry* 2018, 57, 14396–14400.

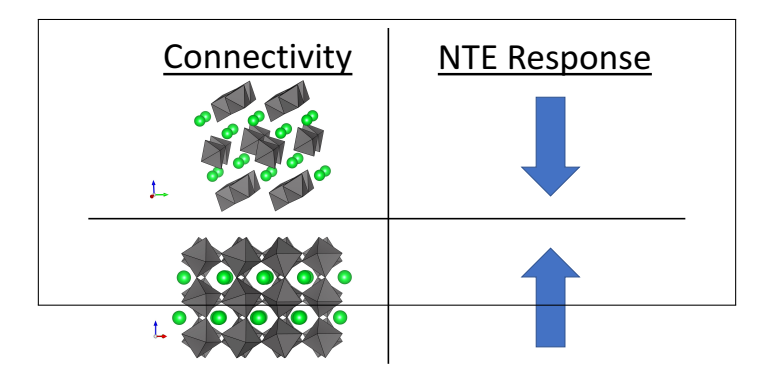
- (23) Yang, C.; Zhang, Y.; Bai, J.; Qu, B.; Tong, P.; Wang, M.; Lin, J.; Zhang, R.; Tong, H.; Wu, Y.; Song, W.; Sun, Y. Crossover of Thermal Expansion From Positive to Negative by Removing the Excess Fluorines in Cubic ReO₃-type TiZrF_{7-x}. J. Mater. Chem. C 2018, 6, 5148–5152.
- (24) Chatterji, T.; Zbiri, M.; Hansen, T. C. Negative thermal expansion in ZnF₂. Applied Physics Letters **2011**, 98, 181911.
- (25) Wang, L.; Yuan, P.-F.; Wang, F.; Sun, Q.; Liang, E.-J.; Jia, Y. Theoretical Study of Negative Thermal Expansion Mechanism of ZnF₂. Materials Research Bulletin 2012, 47, 1113–1118.
- (26) Shi, N.; Song, Y.; Xing, X.; Chen, J. Negative Thermal Expansion in Framework Structure Materials. *Coordination Chemistry Reviews* **2021**, *449*, 214204.
- (27) Huang, L.-F.; Lu, X.-Z.; Rondinelli, J. M. Tunable Negative Thermal Expansion in Layered Perovskites from Quasi-Two-Dimensional Vibrations. *Phys. Rev. Lett.* 2016, 117, 115901.
- (28) Koocher, N. Z.; Huang, L.-F.; Rondinelli, J. M. Negative Thermal Expansion in the Ruddlesden-Popper Calcium Titanates. *Phys. Rev. Materials* **2021**, *5*, 053601.
- (29) Kresse, G.; Furthmüller, J. Efficiency of Ab-Initio Total Energy Calculations for Metals and Semiconductors Using a Plane-Wave Basis Set. *Computational Materials Science* **1996**, *6*, 15–50.
- (30) Kresse, G.; Furthmüller, J. Efficient Iterative Schemes for Ab Initio Total-Energy Calculations Using a Plane-Wave Basis Set. *Phys. Rev. B* **1996**, *54*, 11169–11186.
- (31) Perdew, J. P.; Ruzsinszky, A.; Csonka, G. I.; Vydrov, O. A.; Scuseria, G. E.; Constantin, L. A.; Zhou, X.; Burke, K. Restoring the Density-Gradient Expansion for Exchange in Solids and Surfaces. *Phys. Rev. Lett.* 2008, 100, 136406.

- (32) Blöchl, P. E. Projector Augmented-Wave Method. Phys. Rev. B 1994, 50, 17953–17979.
- (33) Kresse, G.; Joubert, D. From Ultrasoft Pseudopotentials to the Projector Augmented-Wave Method. *Phys. Rev. B* **1999**, *59*, 1758–1775.
- (34) Togo, A.; Tanaka, I. First Principles Phonon Calculations in Materials Science. *Scripta Materialia* **2015**, *108*, 1–5.
- (35) Huang, L.-F.; Lu, X.-Z.; Tennessen, E.; Rondinelli, J. M. An Efficient Ab-Initio Quasi-harmonic Approach for the Thermodynamics of Solids. *Computational Materials Science* **2016**, *120*, 84–93.
- (36) Niu, S.; Milam-Guerrero, J.; Zhou, Y.; Ye, K.; Zhao, B.; Melot, B. C.; Ravichandran, J. Thermal Stability Study of Transition Metal Perovskite Sulfides. *Journal of Materials Research* **2018**, *33*, 4135–4143.
- (37) Dove, M. T.; Fang, H. Negative Thermal Expansion and Associated Anomalous Physical Properties: Review of the Lattice Dynamics Theoretical Foundation. Reports on Progress in Physics 2016, 79, 066503.
- (38) Jaykhedkar, N.; Bystrický, R.; Sýkora, M.; Bučko, T. Understanding the Structure-Band Gap Relationship in SrZrS₃ at Elevated Temperatures: A Detailed *NPT* MD Study. *J. Mater. Chem. C* **2022**, *10*, 12032–12042.
- (39) Huang, L.-F.; Zeng, Z. Roles of Mass, Structure, and Bond Strength in the Phonon Properties and Lattice Anharmonicity of Single-Layer Mo and W Dichalcogenides. The Journal of Physical Chemistry C 2015, 119, 18779–18789.
- (40) Ablitt, C.; Craddock, S.; Senn, M. S.; Mostofi, A. A.; Bristowe, N. C. The Origin of Uniaxial Negative Thermal Expansion in Layered Perovskites. *npj Computational Materials* **2017**, *3*, 44.

- (41) Ritz, E. T.; Benedek, N. A. Interplay Between Phonons and Anisotropic Elasticity Drives Negative Thermal Expansion in PbTiO₃. Phys. Rev. Lett. **2018**, 121, 255901.
- (42) Baxter, S. J.; Loske, K. V.; Lloyd II, A. J.; Wilkinson, A. P. Controlling the Phase Behavior of Low and Negative Thermal Expansion ReO₃-Type Fluorides using Interstitial Anions: Sc_{1-x}Zr_xF_{3+x}. *Inorganic Chemistry* **2020**, *59*, 7188–7194.
- (43) Wang, T.; Xu, J.; Hu, L.; Wang, W.; Huang, R.; Han, F.; Pan, Z.; Deng, J.; Ren, Y.; Li, L.; Chen, J.; Xing, X. Tunable Thermal Expansion and Magnetism in Zr-doped ScF₃. Applied Physics Letters 2016, 109, 181901.
- (44) Ablitt, C.; McCay, H.; Craddock, S.; Cooper, L.; Reynolds, E.; Mostofi, A. A.; Bristowe, N. C.; Murray, C. A.; Senn, M. S. Tolerance Factor Control of Uniaxial Negative Thermal Expansion in a Layered Perovskite. *Chemistry of Materials* **2020**, *32*, 605–610.
- (45) Hancock, J. C.; Chapman, K. W.; Halder, G. J.; Morelock, C. R.; Kaplan, B. S.; Gallington, L. C.; Bongiorno, A.; Han, C.; Zhou, S.; Wilkinson, A. P. Large Negative Thermal Expansion and Anomalous Behavior on Compression in Cubic ReO3-Type A^{II}B^{IV}F₆: CaZrF₆ and CaHfF₆. Chemistry of Materials **2015**, 27, 3912–3918.
- (46) Hester, B. R.; Hancock, J. C.; Lapidus, S. H.; Wilkinson, A. P. Composition, Response to Pressure, and Negative Thermal Expansion in MIIBIVF6 (M = Ca, Mg; B = Zr, Nb). Chemistry of Materials 2017, 29, 823–831.
- (47) Hester, B. R.; Wilkinson, A. P. Negative Thermal Expansion, Response to Pressure and Phase Transitions in CaTiF6. *Inorganic Chemistry* **2018**, *57*, 11275–11281.
- (48) Hester, B. R.; Wilkinson, A. P. Effects of Composition on Crystal Structure, Thermal Expansion, and Response to Pressure in ReO₃-type MNbF₆(M=Mn and Zn). *Journal of Solid State Chemistry* **2019**, *269*, 428–433.

- (49) Lloyd, A. J. I.; Masterson, E. B.; Baxter, S. J.; Molaison, J. J.; dos Santos, A. M.; Wilkinson, A. P. Thermal Expansion and Response to Pressure of Double-ReO3-Type Fluorides NaMVF6 (M = Nb, Ta). *Inorganic Chemistry* 2020, 59, 13979–13987.
- (50) Ni, J. E.; Case, E. D.; Schmidt, R. D.; Wu, C.-I.; Hogan, T. P.; Trejo, R. M.; Kirkham, M. J.; Lara-Curzio, E.; Kanatzidis, M. G. The Thermal Expansion Coefficient as a Key Design Parameter for Thermoelectric Materials and Its Relationship to Processing-Dependent Bloating. *Journal of Materials Science* 2013, 48, 6233–6244.
- (51) Osei-Agyemang, E.; Adu, C. E.; Balasubramanian, G. Ultralow Lattice Thermal Conductivity of Chalcogenide Perovskite CaZrSe₃ Contributes to High Thermoelectric Figure of Merit. *npj Computational Materials* **2019**, *5*, 116.
- (52) Osei-Agyemang, E.; Balasubramanian, G. Understanding the Extremely Poor Lattice Thermal Transport in Chalcogenide Perovskite BaZrS₃. ACS Applied Energy Materials 2020, 3, 1139–1144.
- (53) Osei-Agyemang, E.; Koratkar, N.; Balasubramanian, G. Examining the Electron Transport in Chalcogenide Perovskite BaZrS₃. J. Mater. Chem. C **2021**, 9, 3892–3900.
- (54) Osei-Agyemang, E.; Enninful Adu, C.; Balasubramanian, G. Doping and Anisotropy-Dependent Electronic Transport in Chalcogenide Perovskite CaZrSe₃ for High Thermoelectric Efficiency. *Advanced Theory and Simulations* **2019**, 2, 1900060.
- (55) Song, X.; Shai, X.; Deng, S.; Wang, J.; Li, J.; Ma, X.; Li, X.; Wei, T.; Ren, W.; Gao, L.; Fu, Y.; Wang, H.; Zeng, C. Anisotropic Chalcogenide Perovskite CaZrS₃: A Promising Thermoelectric Material. The Journal of Physical Chemistry C 2022, 126, 11751–11760.

Table of Contents Entry



Edge-shared (α) and corner-shared (β) SrZrS $_3$ exhibit pressure-induced negative thermal expansion (NTE), with the β polymorph exhibiting a higher NTE response owing to its more flexible octahedra.